PCCP

ROYAL SOCIETY OF CHEMISTRY

PAPER

View Article Online
View Journal | View Issue

Cite this: *Phys. Chem. Chem. Phys.*, 2021, **23**, 21959

Structural determination of arginine-linked cisplatin complexes *via* IRMPD action spectroscopy: arginine binds to platinum *via* NO^- binding mode†

C. C. He, [a] L. A. Hamlow, [a] B. Kimutai, [a] H. A. Roy, [a] Zachary J. Devereaux, [a] N. A. Cunningham, [a] J. Martens, [b] G. Berden, [b] J. Oomens, [bc] C. S. Chow [a] and M. T. Rodgers *[a]

Cisplatin, $(NH_3)_2PtCl_2$, has been known as a successful metal-based anticancer drug for more than half a century. Its analogue, Argplatin, arginine-linked cisplatin, $(Arg)PtCl_2$, is being investigated because it exhibits reactivity towards DNA and RNA that differs from that of cisplatin. In order to understand the basis for its altered reactivity, the deprotonated and sodium cationized forms of Argplatin, $[(Arg\text{-}H)PtCl_2]^-$ and $[(Arg)PtCl_2 + Na]^+$, are examined by infrared multiple photon dissociation (IRMPD) action spectroscopy in the IR fingerprint and hydrogen-stretching regions. Complementary electronic structure calculations are performed using density functional theory approaches to characterize the stable structures of these complexes and to predict their infrared spectra. Comparison of the theoretical IR spectra predicted for various stable conformations of these Argplatin complexes to their measured IRMPD spectra enables determination of the binding mode(s) of Arg to the Pt metal center to be identified. Arginine is found to bind to Pt in a bidentate fashion to the backbone amino nitrogen and carboxylate oxygen atoms in both the $[(Arg\text{-}H)PtCl_2]^-$ and $[(Arg)PtCl_2 + Na]^+$ complexes, the NO^- binding mode. The neutral side chain of Arg also interacts with the Pt center to achieve additional stabilization in the $[(Arg\text{-}H)PtCl_2]^-$ complex. In contrast, Na^+ binds to both chlorido ligands in the $[(Arg)PtCl_2 + Na]^+$ complex and the protonated side chain of Arg is stabilized *via* hydrogen-bonding interactions with the carboxylate moiety. These findings are consistent with condensed-phase results, indicating that the NO^- binding mode of arginine to Pt is preserved in the electrospray ionization process even under variable pH and ionic strength.

Received 25th July 2021,
Accepted 17th September 2021

DOI: 10.1039/d1cp03407c

rsc.li/pccp

Introduction

Cisplatin (*cis*-diamminedichloroplatinum, Fig. 1) was first discovered as an anticancer drug in 1965.[1,2] It has been FDA approved and employed to treat a variety of cancers including: testicular, ovarian, cervical, head, neck, bladder, and lung cancers.[3,4] The pharmacological mechanism for cisplatin has been historically identified as its ability to coordinate to and crosslink genomic DNA thereby preventing repair, inhibiting synthesis, and leading to permanent damage that subsequently induces apoptosis in cancer cells. Cisplatin favors binding to the N7 position of purine bases, with a strong preference for guanine over adenine.[5–7] Previous studies indicate that RNA is also a competitive target for cisplatin.[8] Moreover, platinum agents have been shown to exhibit higher reactivity with RNA than DNA oligonucleotides in a salt dependent manner.[9] The reactivity of cisplatin is believed to be a consequence of the lability of its chlorido ligands, which is a prominent factor in determining the rate of adduct formation; whereas the ammonia molecules are carrier ligands that are responsible for producing structurally different DNA adducts.[10–12]

Despite its success, cisplatin suffers from resistance and low cell accumulation due to its reactivity with thiol-containing molecules that may be present at relatively higher levels in cancerous than healthy cells.[13,14] Cisplatin generally produces mild side effects such as nausea and vomiting, but may also cause severe side effects such as neurotoxicity, nephrotoxicity, and emetogenesis.[10,15,16] To overcome side effects associated with cisplatin treatment, cisplatin derivatives involving modification of the chlorido ligands have been examined. Carboplatin, another FDA approved platinum-based anticancer drug, is one such example in which the chlorido ligands of

[a] *Department of Chemistry, Wayne State University, Detroit, Michigan 48202, USA. E-mail: mrodgers@chem.wayne.edu; Tel: +31-(313)577-2431*
[b] *Radboud University, Institute for Molecules and Materials, FELIX Laboratory, Toernooiveld 7, 6525ED Nijmegen, The Netherlands*
[c] *van't Hoff Institute for Molecular Sciences, University of Amsterdam, The Netherlands*

† Electronic supplementary information (ESI) available. See DOI: 10.1039/d1cp03407c

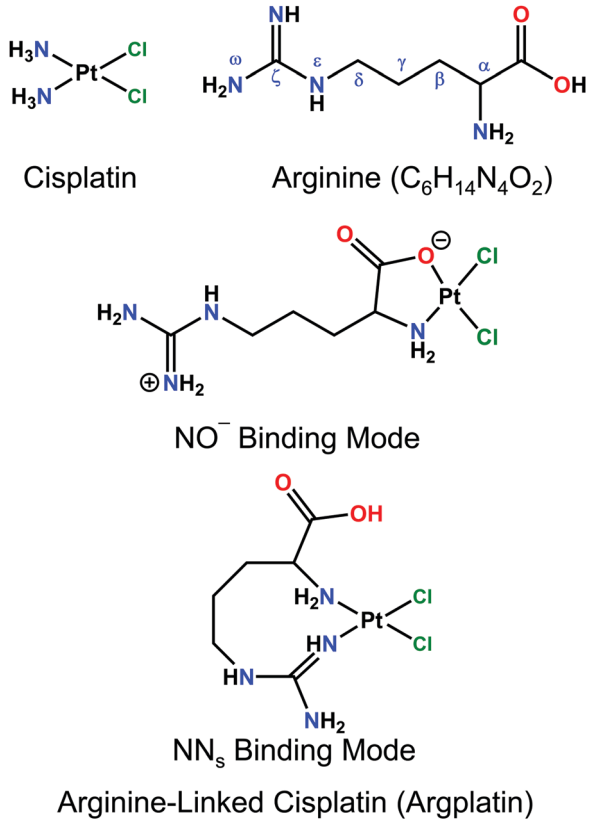

Fig. 1 Chemical structures of cisplatin and schematic diagrams of the NO^- and NNs binding modes of the arginine-linked cisplatin complex (Argplatin) in which arginine binds in a *cis* bidentate fashion to the Pt metal center. The structure of arginine along with designations of the side chain atoms is also shown.

cisplatin have been replaced by a 1,1-cyclobutanedicarboxylato ligand. The resulting change in reactivity is sufficient to eliminate nephrotoxicity in standard doses of carboplatin.[17] Other cisplatin derivatives involving modification of the ammonia ligands such as picoplatin in which one of the ammonia ligands has been replaced by 2-methylpyridine have also been investigated and found to yield a reduced toxicity profile.[18]

Amino acid-linked cisplatin analogues replace both ammonia ligands by coordinating an amino acid to the Pt center. All amino acids possess backbone nitrogen and oxygen atoms that may serve as potential binding sites. The variety of side-chain types present among canonical and noncanonical amino acids also provide additional chelating groups that can be employed to provide another level of diversity to their reaction profiles.[19] In the screening of a solution-phase mixture of 17 amino acid-linked cisplatin derivatives, Lysplatin (lysine-linked cisplatin) exhibited outstanding reactivity with adduct formation observed at all d(AG) and d(GG) sites along the 82mer DNA examined, and with a coordination preference that differs from that of cisplatin where reactivity at d(GG) sites is favored.[20] Argplatin (arginine-linked cisplatin) also exhibited reactivity and cytotoxicity parallel to that of Lysplatin after adjusting the method of synthesis and crystallization.[21] Interestingly, when reacted with ribosomal RNA (rRNA), Argplatin exhibited very different binding preferences, at r(AG) and r(GA) sites, than Lysplatin and Ornplatin (ornithine-linked cisplatin).[22] In particular, Argplatin showed a strong preference for a three-nucleotide bulge region, and less reactivity at the sites where Lysplatin or Ornplatin coordinate preferentially. X-ray crystallography results indicate that Argplatin, Lysplatin, and Ornplatin all coordinate to Pt *via* the backbone nitrogen and oxygen atoms, yet the reactivity of Argplatin clearly differs from that of Ornplatin and Lysplatin.[20–23] In a recent study with prostate cancer cells, Argplatin exhibited outstanding reactivity.[24] The bulky guanidino side chain of Arg is likely responsible for the observed difference in reactivity as it provides the opportunity for potentially different interactions with the nucleotides.

To better understand the differing reactivity of Argplatin *vs.* that of Ornplatin and Lysplatin, we have undertaken a series of investigations to characterize the structures of these amino acid-linked platinum complexes in the gas phase *via* infrared multiple photon dissociation (IRMPD) action spectroscopy techniques complemented and enhanced by electronic structure calculations. Notably, these studies allow detailed examination of the intrinsic structural differences among these complexes without interference from the effects of solvent. The simplest amino acid-linked platinum complex, Glyplatin, $(Gly)PtCl_2$, was first evaluated in its deprotonated form, $[(Gly\text{-}H)PtCl_2]^-$, in our previous work.[25] A variety of binding modes of Gly to Pt were examined, with bidentate coordination to the backbone nitrogen and carboxylate oxygen atoms, the NO^- binding mode, found to be the only mode of binding populated in the experiments. A series of theoretical approaches were evaluated for their performance in properly describing the IR spectrum of $[(Gly\text{-}H)PtCl_2]^-$. Building on knowledge obtained in that study, Argplatin is investigated in this work to provide information regarding the influence of the side chain on the binding. The side chain provides additional potential binding sites to the Pt metal center. Its acyl chain is also long enough to allow other stabilizing interactions such as hydrogen bonds between the guanidino group and the backbone amino or carboxylic acid moieties or the chlorido ligands of the Pt center. In the present work, the deprotonated and sodium cationized forms of Argplatin, $[(Arg\text{-}H)PtCl_2]^-$ and $[(Arg)PtCl_2 + Na]^+$, are examined to mimic the native neutral Argplatin structure produced by crystallization, and to evaluate the stability of the mode of Arg–Pt binding in different pH and ionic strength environments.[21] The structural and energetic information garnered from the calculations enable comprehensive evaluation of the relative stability of all possible modes of binding of Arg to the Pt center, with the deprotonated and sodium cationized complexes elucidating the influence of the local environment on the mode of binding, and comparisons with measured IRMPD spectra establishing the stable low-energy conformers populated in the experiments.

Experimental and computational methods

IRMPD action spectroscopy

Argplatin was synthesized and purified using procedures reported previously.[16,22,24,26] IRMPD action spectra of

$[(\text{Arg-H})PtCl_2]^-$ and $[(\text{Arg})PtCl_2 + Na]^+$ in the fingerprint region were acquired using a modified 3D quadrupole ion trap mass spectrometer (Bruker, AmaZon Speed ETD, Billerica, MA), coupled to the tunable free electron laser (FELIX, Nijmegen, the Netherlands). The experimental setup has been described in detail elsewhere.[27–29] The mechanism of IRMPD involves multiple cycles of photon absorption by a resonant vibrational mode of the ion, rapid redistribution of the absorbed photon energy into the bath of internal modes available to the ion with concomitant relaxation of the excited vibrational mode to its ground state, thereby facilitating additional photon absorption, and culminating in dissociation of the ion, typically *via* the lowest energy dissociation pathway(s) available. The deprotonated complex, $[(\text{Arg-H})PtCl_2]^-$, was generated using an electrospray ionization (ESI) source from a solution containing 10 μM Argplatin in a 50 : 50 (v/v) $MeOH : H_2O$ mixture. The sodium cationized complex, $[(\text{Arg})PtCl_2 + Na]^+$, was generated in an analogous fashion by addition of 10 μM NaCl to the analyte solution.

In separate experiments, the deprotonated and sodium cationized Argplatin complexes were transmitted into the ion trap, where they were mass isolated and irradiated by the free electron laser (FEL) for 180 ms. The FELIX free electron laser provides pulse energies of 20–60 mJ per 5–10 μs macropulse at a 10 Hz repetition rate and with an ~0.4% bandwidth.[27,30] During each experiment, two macropulses were applied in each scan to ensure sufficient photon absorption to induce dissociation, and eight mass scans were averaged at each IR frequency setting. The IR laser frequency in the fingerprint region is calibrated using a grating spectrometer. IRMPD spectra of $[(\text{Arg-H})PtCl_2]^-$ in the frequency range of ~600–1850 cm^{-1} with 0–8 dB attenuation and $[(\text{Arg})PtCl_2 + Na]^+$ in the range of ~600–1900 cm^{-1} with 0–5 dB attenuation were collected several times to validate and compensate for power saturation. The spectra were spliced together with appropriate scaling to correct for differences in power. The resultant spectra were compared with theoretically predicted IR spectra to determine the structures contributing to the measured IRMPD spectra. The original experimental IRMPD spectra with the corresponding attenuation are shown in Fig. S1 (ESI†).

The IRMPD spectra in the hydrogen-stretching region for $[(\text{Arg-H})PtCl_2]^-$ (3000–3700 cm^{-1}) and $[(\text{Arg})PtCl_2 + Na]^+$ (3200–3700 cm^{-1}) were collected on a roughly equivalent modified 3D quadrupole ion trap mass spectrometer (Bruker, AmaZon ETD, Billerica, MA) located at Wayne State University, coupled to a YAG-pumped (Continuum Laser, San Jose, CA) tunable IR OPO/OPA (optical parametric oscillator/amplifier) system (LaserVision, Belleview, WA, USA). The IRMPD spectrum of $[(\text{Arg-H})PtCl_2]^-$ was acquired with a 2 s irradiation time, corresponding to 20 laser pulses, and 10 mass scans were averaged at each IR frequency setting. The IRMPD spectrum of $[(\text{Arg})PtCl_2 + Na]^+$ was acquired with a 4 s irradiation time window, and three averaged mass scans. The IRMPD yield was calculated using the ratio of the sum of the intensities for all fragment ions *versus* the total ion intensity, as described by eqn (1),

$$\text{IRMPD yield} = \sum I_{fi} \Big/ \left(\sum I_{fi} + I_p \right) \quad (1)$$

where I_{fi} and I_p are the measured ion intensities of the fragment and precursor ions, respectively. The IRMPD yield was also corrected for the frequency-dependent variations in the laser power.

To facilitate spectral interpretation, comparisons to the IRMPD spectrum of $[(\text{Gly-H})PtCl_2]^-$, previously reported are made. We note that the data for the $[(\text{Gly-H})PtCl_2]^-$, complex were acquired on a Fourier transform ion cyclotron resonance mass spectrometer (FT-ICR MS). IRMPD spectra taken on these two platforms are generally similar, because in both cases the ions are in complete isolation. Therefore, the absorption frequencies and dissociation threshold should be unaffected by the instrumental platform. The main difference that may affect the measured spectra lies in the background gas pressure in the two instruments (typically 1×10^{-9} mbar on the FT-ICR MS and 1×10^{-3} mbar on the QIT MS). The elevated pressure in the QIT MS may result in some collisional deactivation competing with IR multiple-photon activation to occur. The result is then that the dissociation threshold may not be reached on weak absorptions, particularly for systems with high thresholds. In this case, weak bands may be unobserved on the QIT MS, whereas these weak transitions are observable on the FT-ICR MS.

Computational details

Based on the findings of previous studies, a wide variety of Argplatin structures involving all plausible bidentate interactions of arginine with the Pt center and with the chlorido ligands bound to Pt in a *cis* configuration were constructed for both $[(\text{Arg-H})PtCl_2]^-$ and $[(\text{Arg})PtCl_2 + Na]^+$,[20,21,23,31,32] to comprehensively examine all possible bidentate modes of binding between Arg and Pt, deprotonation sites, modes of Na^+ binding, as well as hydrogen-bonding interactions.[25,33] The initial structures for these Argplatin complexes were optimized using the B3LYP/mDZP/def2-TZVP hybrid approach as this approach was found to produce the best reproduction of the IRMPD spectrum of the $[(\text{Gly-H})PtCl_2]^-$ complex.[25] In this hybrid approach, the mDZP basis set was used for Pt, while the def2-TZVP basis set was used for all other atoms. The mDZP basis set is an augmented all-electron double zeta polarization basis set, whereas the def2-TZVP basis set is a triple zeta valence polarization basis set. While it might have been anticipated that a balanced basis set would provide better results, we note that for Pt the def2-TZVP basis set is a valence basis set combined with an effective core potential. The quality of the energetic predictions of the hybrid method employed here has not been adequately evaluated yet, but is consistent with the observed IRMPD spectrum of the $[(\text{Gly-H})PtCl_2]^-$ complex.[25] Computations were performed using the Gaussian 09 suite of programs.[33] The nonstandard basis sets were acquired from the EMSL basis set exchange library.[34,35]

The low-energy binding modes of $[(\text{Arg-H})PtCl_2]^-$ and $[(\text{Arg})PtCl_2 + Na]^+$ as shown in Fig. S2 and S3 (ESI†) were subjected to further molecular mechanics (MM) calculations

using HyperChem software, to relax the floppy side chain of arginine and explore the conformational space available to that structure.[36] Due to the lack of parameters for Pt in the AMBER force field, the MM+ force field, which is derived from the MM2 force field, was employed in the simulated annealing process.[37–40] Additional parameters such as the Pt–O bond length and bond angles involving the Pt–O bond were derived from the density functional theory calculations performed on the initial structures described above. Existing parameters reported in the literature for Pt–N were used for the other Pt–O related parameters required.[39,40] The simulated annealing procedure employed here parallels that used in our previous IRMPD studies.[41–49] In brief, each initial structure was subjected to an annealing process with the temperature ramped from 0 to 1000 K in 0.3 ps, held at 1000 K for 0.2 ps to allow the complex to sample conformational space, and then cooled down to 0 K in 0.3 ps. This annealing process was repeated for 300 cycles for each initial structure examined. To maintain an approximately square planar shape of the Pt coordination sphere, energy restrictions on the bond and dihedral angles involving the Pt center were applied to the structures. For instance, in the setup for the NO^- binding mode of $[(Arg\text{-}H)PtCl_2]^-$, the $\angle NPtCl_b$ and $\angle OPtCl_O$ angles and the $\angle NPtOCl_b$ and $\angle OPtNCl_O$ dihedral angles were constrained, where Cl_b is the chloride *trans* to the backbone nitrogen and Cl_O is the chloride *trans* to the backbone oxygen. The starting parameters of these angles and dihedral angles were taken from the initial structure, and their force constants were set to a reasonably large value (1000 kcal mol^{-1} $Å^{-2}$) to maintain the square planar shape of the Pt coordination sphere during the annealing process.

Thirty of the 300 candidate structures generated for each unique binding mode were selected based on their relative energies calculated at the molecular mechanics level and re-optimized at B3LYP/mDZP/def2-TZVP level of theory. Relative Gibbs energies at 298 K and the linear IR spectra predicted for these representative conformers were extracted and compared with the measured IRMPD spectra. Based on previous results for $[(Gly\text{-}H)PtCl_2]^-$,[25] the computed frequencies were scaled by a factor of 0.970 and convoluted over a Gaussian line shape having a full width at half max (fwhm) of 20 cm^{-1} in the IR fingerprint region. In the hydrogen-stretching region, computed frequencies were scaled by 0.957 and convoluted with a Gaussian line shape having a fwhm of 10 cm^{-1} to generate the theoretical spectra.

Results

IRMPD action spectroscopy

As a derivative of cisplatin, it may be anticipated that Argplatin would exhibit parallel reactivity with DNA or RNA. Hence, studying the intrinsic fragmentation pathways of Argplatin in the gas phase may provide insight into its reactivity in solution. Photodissociation of the $[(Arg\text{-}H)PtCl_2]^-$ and $[(Arg)PtCl_2 + Na]^+$ complexes occurs along many pathways as summarized in Table 1; the diversity partially afforded by the guanidino group of the Arg side chain. Notably, a larger variety of photodissociation pathways are observed in the IR fingerprint region than in the hydrogen-stretching region. The enhanced reactivity in the IR fingerprint region can likely be attributed to more extensive sequential fragmentation induced by the enhanced power provided by the FEL. The major fragmentation pathway observed for both complexes involves neutral loss of HCl. Neutral loss of a second HCl molecule was also observed in both spectral regions. Such facile elimination of the chlorido ligands is consistent with the currently accepted mechanism behind the reactivity of cisplatin.[10–12] Further discussion of the mechanisms associated with the intrinsic fragmentation pathways of $[(Arg\text{-}H)PtCl_2]^-$ and $[(Arg)PtCl_2 + Na]^+$ is deferred to the discussion section in order to provide an appropriate overview once the conformations populated in the experiments have been deduced based on spectroscopic comparisons.

The measured IRMPD spectra of the $[(Arg–H)PtCl_2]^-$ and $[(Arg)PtCl_2 + Na]^+$ complexes are compared to that of the $[(Gly\text{-}H)PtCl_2]^-$ complex[25] in Fig. 2. To facilitate comparisons, weak spectral features that appear in the low-frequency range of the fingerprint region of the $[(Arg\text{-}H)PtCl_2]^-$ and $[(Arg)PtCl_2 + Na]^+$ spectra have been amplified by a factor of five. The dominant features in both the IR fingerprint region at ~1650 cm^{-1} and hydrogen-stretching region at ~3350 cm^{-1} of the IRMPD spectrum of $[(Gly\text{-}H)PtCl_2]^-$ are also preserved in the spectra of the $[(Arg\text{-}H)PtCl_2]^-$ and $[(Arg)PtCl_2 + Na]^+$ complexes. However, the feature at ~1650 cm^{-1} exhibits extensive broadening in the spectra of both Argplatin complexes, and the feature at

Table 1 Fragment ions observed upon IRMPD of Argplatin complexes in the fingerprint and hydrogen-stretching regions[a]

Precursor/ product ion	*m/z* (exact)	*m/z* (FEL)	*m/z* (OPO)	Neutral losses
$[(Arg–H)PtCl_2]^-$				
$C_6H_{13}N_4O_2Cl_2Pt$	438.0063	437.8	437.9	
$C_6H_{12}N_4O_2ClPt$	402.0297	401.8	401.9	HCl
$C_6H_9N_3O_2ClPt$	385.0031	384.8		$HCl + NH_3$
$C_5H_8NO_2Cl_2Pt$	378.9580	378.7	378.9	CN_3H_5
$C_6H_{11}N_4O_2Pt$	366.0530	365.8	365.9	2HCl
$C_6H_9N_4O_2Pt$	364.0373	363.8		$2HCl + H_2$
$C_5H_{10}N_4ClPt$	356.0242	355.8	355.9	$HCl + CO + H_2O$
$C_6H_8N_3O_2Pt$	349.0264	348.8		$2HCl + NH_3$
$C_5H_7NO_2ClPt$	342.9813	342.7	342.9	$HCl + CN_3H_5$
$C_5H_9N_4Pt$	320.0475	319.8		$2HCl + CO + H_2O$
$C_5H_7N_4Pt$	318.0318	317.8		$2HCl + CO + H_2O + H_2$
C_4H_5NClPt	296.9758	296.6		$HCl + CO + H2O + CN_3H_5$
CHNClPt	256.9445	256.5		$HCl + CO_2 + N_3H_5 + C_3H_6$
$[(Arg)PtCl_2 + Na]^+$				
$C_6H_{14}N_4O_2Cl_2PtNa$	462.0039	461.8	461.9	
$C_6H_{12}N_4OCl_2PtNa$		443.8	443.9	H_2O
$C_6H_{13}N_4O_2ClPtNa$		425.9	426.0	HCl
$C_6H_{10}N_3O_2ClPtNa$		408.9		$HCl + NH_3$
$C_6H_{11}N_4OClPtNa$		407.9	407.9	$H_2O + HCl$
$C_5H_9NO_2Cl_2PtNa$		402.8		CN_3H_5
$C_5H_8NO_2Cl_2PtNa$		401.8	401.9	$H_2O + HN{=}C{=}NH$
$C_6H_{12}N_4O_2PtNa$		389.9	390.0	2HCl
$C_6H_9N_3O_2PtNa$		372.9		$2HCl + NH_3$

[a] Note that the differences between the exact *m/z* and the *m/z* of the precursor and product ions meausred in the experiments is associated with the limited *m/z* accuracy of the QIT MS instruments.

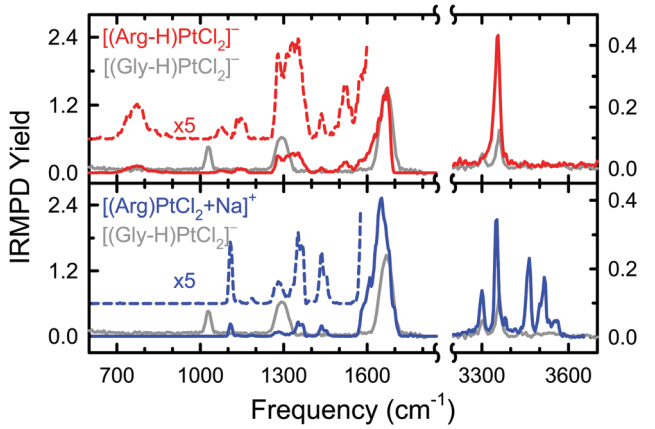

Fig. 2 Experimental IRMPD spectra of the $[(Arg\text{-}H)PtCl_2]^-$ and $[(Arg)PtCl_2 + Na]^+$ complexes over the IR fingerprint (600–1850 cm^{-1}) and hydrogen-stretching (3200–3700 cm^{-1}) regions. Spectral features in the low-frequency region of the spectra have been amplified and offset from baseline to enhance visualization of the weak features observed in this region. The IRMPD spectrum of $[(Gly\text{-}H)PtCl_2]^-$ previously reported is overlaid in gray for comparison and taken from ref. 25.

$\sim$3350 cm^{-1} is significantly broadened in the IRMPD spectrum of the $[(Arg\text{-}H)PtCl_2]^-$ complex. Other similarities in the spectra are evident. Notably, all exhibit broad features at $\sim$1300 cm^{-1}. However, these features exhibit more extensive broadening and their shapes suggest that three or four distinct vibrational modes contribute to these features in the spectra for both Argplatin complexes, whereas the symmetric shape of this band for the $[(Gly\text{–}H)PtCl_2]^-$ complex suggests at it arises from a single vibrational mode. Likewise, all three complexes exhibit a weak feature at $\sim$3300 cm^{-1}; however, this feature appears as a shoulder to the red of the feature at $\sim$3350 cm^{-1} in the $[(Arg\text{-}H)PtCl_2]^-$ spectrum due to the extensive broadening of that peak. The most notable difference in the spectra of the $[(Gly\text{–}H)PtCl_2]^-$ and $[(Arg\text{–}H)PtCl_2]^-$ complexes *vs.* that of $[(Arg)PtCl_2 + Na]^+$ is seen in the complexity of the hydrogen-stretching region where the $[(Arg)PtCl_2 + Na]^+$ complex exhibits a much richer variety of hydrogen stretches. The spectral differences in this region are likely attributable to the absence of a side chain in the $[(Gly\text{–}H)PtCl_2]^-$ complex, and differences in the state of protonation of the amino acid (deprotonated *vs.* neutral zwitterionic) in the $[(Arg\text{-}H)PtCl_2]^-$ and $[(Arg)PtCl_2 + Na]^+$ complexes that in turn lead to different opportunities for hydrogen-bonding interactions involving the guanidino side chain. The more complex spectrum observed for the $[(Arg)PtCl_2 + Na]^+$ complex may also arise from the population of multiple conformers in the experiments.

Nomenclature

The modes of binding of Arg to Pt in the $[(Arg\text{-}H)PtCl_2]^-$ and $[(Arg)PtCl_2 + Na]^+$ complexes are classified by their Pt chelating mode. If the binding mode to Pt involves a deprotonated or protonated site, it is indicated with a negative or positive sign, respectively. The backbone nitrogen is simply denoted as N, the most plausible chelating side chain nitrogen atom is designated as N_s, whereas the other side chain nitrogen atoms are denoted as N_ω and N_ε-based on their position along the side chain, see Fig. 1. The flexibility of the Arg side chain enables the formation of multiple stable conformers for each binding mode. The stable conformers found for each binding mode are further designated with an underscore and a letter. The ground conformer is designated with an A, whereas excited conformers are designated with a letter (or letters) that are alphabetically incremented based on their relative Gibbs energies, *i.e.*, A, B, C, *etc.* In virtually all of the stable conformers determined for the $[(Arg)PtCl_2 + Na]^+$ complex, the sodium cation binds between the two chlorido ligands. For these stable conformers no specific designation of the sodium cation binding mode is given. For the handful of conformers where the sodium cation binding mode differs, the Pt chelating mode is followed by an underscore and then the sodium chelating mode is given. When the sodium cation binding mode involves one or more of the chlorido ligands, they are denoted with a subscript that indicates the atom that it is *trans* to (*e.g.*, Cl_b, Cl_O, and Cl_s denote Cl being *trans* to the backbone nitrogen, the carboxyl/carboxylate oxygen, and side chain nitrogen atoms, respectively). The two most favorable low-energy binding modes of the $[(Arg\text{–}H)PtCl_2]^-$ and $[(Arg)PtCl_2 + Na]^+$ complexes, NN_s and NO^-, are shown schematically in Fig. 1, whereas all low-energy binding modes are shown in Fig. S2 and S3 (ESI†), along with the naming designations.

Stable structures of the $[(Arg\text{-}H)PtCl_2]^-$ complex

To fully explore the conformational space available to the $[(Arg\text{-}H)PtCl_2]^-$ complex, candidate structures were constructed and subjected to simulated annealing to allow relaxation of the Arg side chain as described in the Computational details section. The stable low-energy structures found for the $[(Arg\text{-}H)PtCl_2]^-$ complex are compared in Fig. S4 (ESI†). Interestingly, the calculations predict that two different conformers of the $[(Arg\text{-}H)PtCl_2]^-$ complex, **NN_s_A** and **NO^-_A** that involve distinct modes of binding, are equally stable such that they are both ground structures. Further, all stable NN_s and NO^- conformers found are predicted to be relatively low in Gibbs energy *vs.* the other modes of binding. In the NN_s binding structures, several modes of hydrogen bonding between the carboxylate group and the backbone amino or side chain guanidino moieties to enhance stabilization are found. When extended, the side chain guanidino moiety can even form a hydrogen bond with one of the chlorido ligands, see for example the **NN_s_K** conformer of Fig. S4 (ESI†). The NO^- binding mode provides even more side chain flexibility to Arg and allows hydrogen-bonding interactions between the guanidino group and the carboxylate group, Pt, or the chlorido ligands, see conformers **NO^-_B**, **NO^-_A**, and **NO^-_T**, of Fig. S4 (ESI†). In some cases, multiple hydrogen bonds are formed between the guanidino and carboxylate moieties, see conformer **NO^-_K**. The N_sO^- binding mode is much less favorable than NO^-. The most stable N_sO^--conformer found, **N_sO^-_A**, is predicted to be 25.1 kJ mol^{-1} less stable than the ground conformers even though the delocalized π bond is maintained in this structure. The OO^- binding mode has previously shown to be the preferred mode of binding of Cs^+ to several amino acids.[50–52] However, the most

stable OO^- binding conformer of $[(Arg–H)PtCl_2]^-$, **OO^-_A**, is predicted to be 71.8 kJ mol^{-1} less stable than the ground conformers due to the destabilization arising from the unfavorable ∠OPtO angle associated with the mode of binding. Likewise, stable conformers involving interaction with the less favorable side chain nitrogen atoms exhibit relative higher Gibbs energies than the NN_s and NO^- binding conformers. The most stable conformers of each binding type, **NN_ε_A**, **NN_ω_A**, **$N_\omega O^-$_A**, and **$N_\varepsilon O^-$_A**, are less stable than the ground conformers by 23.9, 26.7, 32.8, and 57.2 kJ mol^{-1}, respectively. The decreased stability of these latter conformers is likely due to the disruption of the delocalized π bond of the guanidino moiety. Overall, the NN_s and NO^- binding modes are energetically favored over all other binding modes. Further, the conformational flexibility of the Arg side chain *vs.* the backbone leads to many more low-energy conformers involving the NO^- binding mode than the NN_s binding mode. Indeed, only seven NN_s *vs.* 37 NO^- binding conformers are found within 20 kJ mol^{-1} of the ground **NN_s_A** and **NO^-_A** conformers.

Stable structures of the $[(Arg)PtCl_2 + Na]^+$ complex

For the $[(Arg)PtCl_2 + Na]^+$ complex, the modes of binding of both the Pt and Na cations are of interest. The candidate structures shown in Fig. S3 (ESI†) were constructed and subjected to simulated annealing to allow relaxation of the Arg side chain. The optimized structures are shown in Fig. S5 (ESI†). Parallel to that found for $[(Arg–H)PtCl_2]^-$, the preferred modes of Arg binding to the Pt center are again NN_s and NO^-, with binding of the sodium cation to both chlorido ligands. Thus, many of the stable NN_s and NO^- conformers of $[(Arg)PtCl_2 + Na]^+$ exhibit relatively low Gibbs energies. Indeed, among the stable NN_s and NO^- conformers found, 19 and 18 conformers involving these two binding modes are found within 20 kJ mol^{-1} of the ground **NN_s_A** conformer, respectively. In contrast to $[(Arg–H)PtCl_2]^-$, the most stable NO^- binding conformer found, **NO^-_A** is predicted to be 1.8 kJ mol^{-1} less stable than the ground **NN_s_A** conformer. In the NN_s binding conformers, the carboxylic acid moiety is neutral. Interestingly, when the carboxylic acid moiety is in its neutral form, it is a much poorer binder to Pt such that the most stable NO binding conformer, **NO_A** conformer is 82.3 kJ mol^{-1} less stable than the **NO^-_A** conformer, see Fig. S5 (ESI†). This preference for the zwitterionic form of Arg is not unexpected based on the pK_as of these functional groups (1.823 for the backbone carboxylic acid moiety, 8.991 for the backbone amino group, and 12.1 for the side chain guanidine moiety). In contrast, the neutral form of Arg is preferred in conformers that involve bidentate interactions with the side-chain nitrogen and the backbone oxygen atoms. The most stable N_sO binding conformer found, **N_sO_A**, was computed at 49.8 kJ mol^{-1}, whereas the most stable N_sO^- binding conformer, **N_sO^-_A** conformer, is predicted to lie 16.0 kJ mol^{-1} higher in Gibbs energy, or 65.8 kJ mol^{-1} relative to the ground conformer. These findings indicate that the relative proton affinities of the carboxylate *versus* amino moieties are altered upon binding to Pt. As found for the deprotonated Argplatin complex, the OO^- binding mode is much less favorable due to the unfavorable ∠OPtO angle associated with this mode of binding; the most stable **OO^-_A** conformer found is predicted to be 83.1 kJ mol^{-1} less stable than the ground conformer. Stable conformers involving interaction with the less favorable side chain nitrogen atoms are again predicted to be much less stable than when binding occurs *via* the backbone nitrogen atom. The most stable conformers of each binding type, **NN_ε_A**, **NN_ω_A**, **$N_\omega O$_A**, and **$N_\varepsilon O$_A**, are less stable than the ground conformer by 67.7, 80.1, 121.2, and 145.9 kJ mol^{-1}, respectively. The decreased stability of these latter conformers is likely due to the disruption of the delocalized π bond of the guanidino moiety.

As indicated above, bidentate interaction of the sodium cation with the chlorido ligands is favored over other sodium cation binding modes. For example, the **NN_s_OCl_bCl_s_A** and **NN_s_OCl_s_A** conformers lie 36.7 and 69.2 kJ mol^{-1} higher in Gibbs energy than the **NN_s_A** conformer, see the other binding modes of Fig. S5 (ESI†). Parallel results are found in other cases. Compare the **NO^-_OCl_b_A** and **NO^-_A** conformers, the **N_sO^-_OCl_s_A** and **N_sO^-_A** conformers, and the **NO_$N_sCl_bCl_O$_A** and **NO_A** conformers, where bidentate binding of the sodium cation to the chlorido ligands is favored by 19.6, 31.9, and 2.4 kJ mol^{-1}, respectively. In summary, NN_s and NO^- binding modes are energetically favored over all other binding modes.

Discussion

Interpretation of the experimental IRMPD action spectra

As discussed above, the structural and energetic information provided by the calculations enables the stability of various modes of binding of Arg to the Pt center to be determined, with the deprotonated and sodium cationized complexes elucidating the influence of the local environment on the binding modes. Comparisons of the experimentally measured IRMPD spectra with theoretical IR spectra predicted for various stable conformations of these Argplatin complexes enables the stable low-energy conformers that are populated in the experiments to be determined. One caveat associated with the use of the harmonic approximation in the computational modeling is that it may lead to significant spectral misalignments between the experimental and the computed IR features involving strong hydrogen-bonding interactions in the hydrogen-stretching region.[53–56] Theory tends to overestimate the intensity of the spectral features arising from such hydrogen bonds, whereas features in the experimental data are usually broadened and much flatter, and red shifted *versus* the harmonic approximation. Unfortunately, current protocols such as the second-order vibrational perturbation theory (VPT2) approach for making anharmonic corrections generally do not improve spectra alignment without heroic efforts and thus were not pursued here.[25]

Structures of the $[(Arg–H)PtCl_2]^-$ complex populated in the experiments

The IR spectra predicted for the ground **NN_s_A** conformers along with the stable NO^- conformers of the $[(Arg–H)PtCl_2]^-$

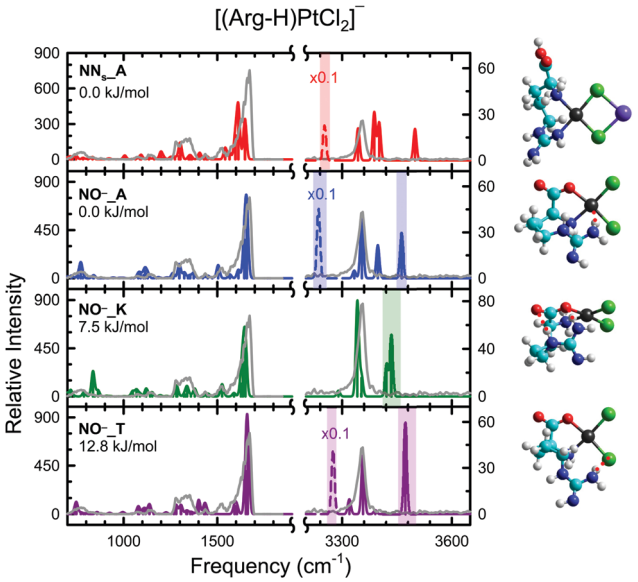

Fig. 3 Comparison of the experimental IRMPD spectrum of the $[(Arg\text{-}H)PtCl_2]^-$ complex with theoretical IR spectra predicted for the **NN_s_A**, **NO^-_A**, **NO^-_K**, and **NO^-_T** conformers along with their optimized structures and relative Gibbs energies calculated at the B3LYP/mDZP/def2-TZVP level of theory at 298 K. The red dotted lines show additional stabilizing interactions between the side chain guanidino moiety and the Pt center, backbone carboxylate, or chlorido ligands. The IR bands highlighted arise from strong hydrogen-bonding interactions that are not well described by theory.

complex that provide the best match to the experimental IRMPD spectrum are compared in Fig. 3. Spectral features that involve strong hydrogen-bonding interactions that are not well described by theory are highlighted. The ground **NN_s_A** conformer exhibits several spectral features that are not well aligned with the measured IRMPD spectrum indicating that this conformer, despite of its low relative Gibbs energy, is not populated in the experiments. The IR spectrum predicted for the ground **NO^-_A** conformer represents the experimental data very well when the highlighted spectral features are excluded from the comparison. Conformers **NO^-_K** (7.5 kJ mol^{-1}) and **NO^-_T** (12.8 kJ mol^{-1}) cannot be ruled out based on their computed IR spectra. However, their relative Gibbs energies suggest that their populations in the experiments are probably much lower than that of the **NO^-_A** conformer. Hence, peak assignments for the $[(Arg\text{–}H)PtCl_2]^-$ complex are based on the **NO^-_A** conformer and are listed in Table 2.

The spectra predicted for other stable conformers of the $[(Arg\text{–}H)PtCl_2]^-$ complex that exhibit alternative platinum binding modes and hydrogen-bonding interactions are also compared to the experimental data in Fig. S6–S10 (ESI†). It is particularly noteworthy that although the calculations indicate that the NN_s mode of binding is relatively favorable, and that the **NN_s_A** conformer in particular is isoenergetic with the **NO^-_A** ground conformer, spectral mismatches in both the fingerprint and hydrogen-stretching regions indicate that NN_s conformers are not measurably populated in the experiments, see Fig. S6 (ESI†). Spectral comparisons for additional select

Table 2 Vibrational band assignments for the $[(Arg\text{-}H)PtCl_2]^-$ complex[a]

Experimental band (cm^{-1})	Vibrational mode
774	N_s–H/N_ω–H_2 wagging
833	CH_2 rocking/wagging
1078	C_ζ–N_ω stretch/N_ω–H_2 rocking/C–H_2 rocking
1147	N_s–H bending/N_ω–H_2 twisting/N–H_2 wagging
1279	C–O(Pt) stretch/C–H_2 twisting
1352	C–H_2 wagging/N–H_2 twisting
1436	C–H_2 bending
1526	C_ζ–N_ε stretch/N_ε–H bending
1672	N_ω–H_2 bending/C_ζ–N_s stretch/C=O stretch
3356	N–H_2 asymmetric stretch/N_s–H stretch
3404	N_ε–H stretch
3448	N_ω–H_2 asymmetric stretch

[a] Band assignments are based on the **NO^-_A** conformer. A scaling factor of 0.970 was used in the fingerprint region (FEL), whereas a scaling factor of 0.957 was used in the hydrogen-stretching region (OPO). See Fig. 1 for the designations.

NO^- conformers that exhibit alternative modes of hydrogen-bond stabilization than the conformers compared in Fig. 3 are shown in Fig. S7 (ESI†). Similarly, spectral comparisons for select N_sO^- binding conformers are provided in Fig. S8 (ESI†). Likewise, spectral comparisons for select OO^- binding conformers are provided in Fig. S9 (ESI†). Finally, spectral comparisons for the ground conformers of various side chain binding modes, **NN_ε_A**, **NN_ω_A**, **$N_\omega O^-$_A**, and **$N_\varepsilon O^-$_A**, are shown in Fig. S10 (ESI†). In all cases, spectral misalignments particularly in the hydrogen-stretching region and differences in the shapes of various spectral features along with higher Gibbs energies indicate that these structures are not measurably populated in the experiments.

Structures of the $[(Arg)PtCl_2 + Na]^+$ complex populated in the experiments

The IR spectra predicted for the ground **NN_s_A** conformer along with the stable NO^- conformers of the $[(Arg)PtCl_2 + Na]^-$ complex that provide the best match to the experimental IRMPD spectrum are compared in Fig. 4. Spectral features that involve strong hydrogen-bonding interactions that are not well described by theory are again highlighted. The ground **NN_s_A** conformer exhibits several spectral features that are not well aligned with the measured IRMPD spectrum indicating that this conformer, despite of its low relative Gibbs energy, is not populated in the experiments. In particular, the **NNs_A** conformer exhibits a free C=O stretch, whereas this typically intense feature is absent in the experimental spectrum. Combined, the predicted IR spectra of the selected NO^- binding conformers displayed in Fig. 4 well represent the experimental spectrum of $[(Arg)PtCl_2 + Na]^+$ in the IR fingerprint region above 1100 cm^{-1} and hydrogen-stretching region. The experimental spectrum does not exhibit any features below 1100 cm^{-1}, whereas the predicted spectra for each of the conformers exhibit minor features in this region. The intense feature at ~1600 cm^{-1} and the small features below 1500 cm^{-1} predicted for the **NO^-_A** and **NO^-_B** (see Fig. S7, ESI†) conformers match the experimental ratio relatively well. These conformers differ only in the orientation of the $N_\omega H_2$ group, which is hard to

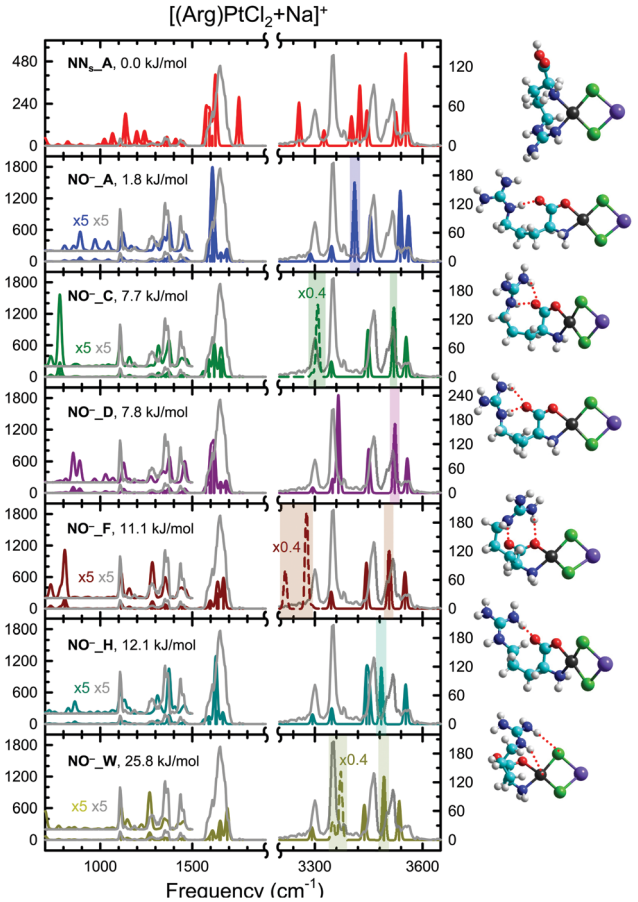

Fig. 4 Comparison of the experimental IRMPD spectrum of $[(Arg)PtCl_2 + Na]^+$ with theoretical IR spectra predicted for the **NN_s_A**, **NO^-_A**, **NO^-_B**, **NO^-_C**, **NO^-_D**, **NO^-_F**, **NO^-_H**, and **NO^-_W** conformers along with their optimized structures and relative Gibbs energies calculated at the B3LYP/mDZP/def2-TZVP level of theory at 298 K. The red dotted lines show additional stabilizing interactions between the side chain guanidino moiety and the backbone carboxylate, Pt center, or chlorido ligands. The IR bands highlighted arise from strong hydrogen-bonding interactions that are not well described by theory.

distinguish from their predicted IR spectra. Their Gibbs energies also differ by only 1.0 kJ mol^{-1}. However, the peak at ~3500 cm^{-1} is not well represented by these two conformers. Conformers **NO^-_C**, **NO^-_D**, and **NO^-_F** provide better agreement with the experimental IRMPD spectrum for the feature at ~1350 cm^{-1} and over the hydrogen-stretching region as a result of the different hydrogen-bonding interactions between the guanidinium and carboxylate moieties present in these conformers. The predicted IR spectrum for the **NO^-_H** conformer provides an even better match to the experimental data in the fingerprint region than the lower-energy conformers although theory suggests that this conformer is 10.3 kJ mol^{-1} less stable than the lowest energy **NO^-_A** conformer. The small feature observed at ~3380 cm^{-1} is only found in the spectrum predicted for the **NO^-_W** conformer, suggesting that this conformer is present in small abundance. Considering the desolvation process that occurs during electrospray ionization (ESI), it is plausible that these various modes of intramolecular hydrogen-bond stabilization could be formed when the side chain folds back on itself seeking stabilization as solvent molecules are removed in the gas phase such that all of these low-energy NO^- binding conformers are populated to varying extents in the experiments. Vibrational band assignments are based primarily on the ground **NO^-_A** conformer, with the feature at 3380 cm^{-1} assigned based on the **NO^-_W** conformer and the feature at 3516 cm^{-1} assigned based on the **NO^-_C**, **NO^-_D**, or **NO^-_F** conformers; results are listed in Table 3.

The IR spectra predicted for other stable conformers of the $[(Arg)PtCl_2 + Na]^+$ complex that exhibit alternative platinum binding modes and hydrogen-bonding interactions are also compared to the measured IRMPD spectrum in Fig. S11–S15 (ESI†). As found for the $[(Arg\text{-}H)PtCl_2]^-$ complex, the NN_s conformers of $[(Arg)PtCl_2 + Na]^+$ lie low in Gibbs energy. Indeed, the **NN_s_A** conformer is predicted to be the ground conformer, and 1.8 kJ mol^{-1} more stable than the **NO^-_A** conformer, see Fig. S5 (ESI†). Yet, spectral mismatches in both the fingerprint and hydrogen-stretching regions indicate that NN_s conformers are not measurably populated in the experiments. See for example, comparisons for the **NN_s_A** and **NN_s_E** conformers shown in Fig. S11 (ESI†). Most notably, the intense C=O stretch of the carboxyl group is predicted to occur at ~1750 cm^{-1}, whereas no feature is observed at this frequency in the measured IRMPD spectrum, indicating that neither of these two conformers are significantly populated in the experiments. Spectral comparisons for additional select NO^- conformers that exhibit alternative modes of hydrogen-bond stabilization than the conformers compared in Fig. 4 are shown in Fig. S12 (ESI†). Similarly, spectral comparisons for select N_sO binding conformers are provided in Fig. S13 (ESI†). Likewise, spectral comparisons for select OO^- binding conformers are provided in Fig. S14 (ESI†). Finally, spectral comparisons for the ground conformers of various side chain and sodium cation binding modes, **NO^-_OCl_b_A**, **NN_s_OCl_bCl_s_A**, **N_sO^-_A**, **NN_ε_A**, **NN_s_OCl_s_A**, **NN_ω_A**, **NO_A**, **NO_$N_sCl_bCl_O$_A**, **N_sO^-_OCl_s_A**, **$N_\omega O$_A**, and **$N_\varepsilon O$_A**, are shown in Fig. S15 (ESI†). In all cases, spectral misalignments particularly in the hydrogen-stretching

Table 3 Vibrational band assignments for $[(Arg)PtCl_2 + Na]^+$ Complex[a]

Experimental band (cm^{-1})	Vibrational mode
1108	N–H_2 wagging
1280	C–H_2 twisting
1352	C–H_2 wagging/N–H_2 twisting/C–O(Pt) stretch
1437	C–H_2 bending
1652	N_ω–H_2/N–H_2/N_ε–H bending/C_ζ–N_ε/C_ζ–N_ω/C=O stretch
3300	N–H_2 symmetric stretch
3352	N–H_2 asymmetric stretch
3380	N_ε–H stretch/N_ω–H_2 (facing O) symmetric stretch[b]
3416	N_ω–H_2 (facing O) symmetric stretch
3464	N_ω–H_2 (facing away) symmetric stretch
3516	N_ω–H_2 (facing O) asymmetric stretch[c]
3560	N_ω–H_2 (facing away) asymmetric stretch

[a] Band assignments are based on the **NO^-_A** conformer. A scaling factor of 0.970 was used in the fingerprint region (FEL), whereas a scaling factor of 0.957 was used in the hydrogen-stretching region (OPO). See Fig. 1 for the designations. [b] Contributed by conformer **NO^-_W**. [c] Contributed by the **NO^-_C**, **NO^-_D**, or **NO^-_F** conformers.

region and differences in the shapes of various spectral features combined with computed higher Gibbs energies indicate that these structures can be eliminated as important contributors to the experimental spectrum.

Fragmentation analysis of the $[(Arg–H)PtCl_2]^-$ and $[(Arg)PtCl_2 + Na]^+$ complexes

IRMPD spectroscopic results suggest that Arg binds to Pt *via* the NO^- binding mode in both $[(Arg–H)PtCl_2]^-$ and $[(Arg)PtCl_2 + Na]^+$. Based on previous studies of protonated and cationized arginine,[57–63] proposed fragmentation pathways of the $[(Arg–H)PtCl_2]^-$ and $[(Arg)PtCl_2 + Na]^+$ complexes are given in Schemes 1 and 2. The major fragmentation pathways are indicated in boldface, whereas the electron transfer (ET) processes are indicated using the color of the corresponding neutral loss. For example, ET processes involved in the loss of HCl are marked in green. Most pathways observed in the IRMPD experiments of Argplatin are parallel to the previous findings in the cases of protonated and cationized arginine or 18-crown-6 captured arginine, except for the unique HCl loss in Argplatin.[57–60,62,64–67] In particular, the loss of one and two HCl molecules are both major dissociation pathways for the $[(Arg–H)PtCl_2]^-$ and $[(Arg)PtCl_2 + Na]^+$ complexes, consistent with the accepted mechanism behind the reactivity of cisplatin.[10–12] Elimination of HCl was also observed as the major fragmentation pathway for the $[(Gly–H)PtCl_2]^-$ complex.[25] Water loss followed by a sequential elimination of HN=C=NH or HCl was observed as a dominant fragmentation pathway for $[(Arg)PtCl_2 + Na]^+$, but does not occur for $[(Arg–H)PtCl_2]^-$. The water loss is probably due to the zwitterionic tautomerization of

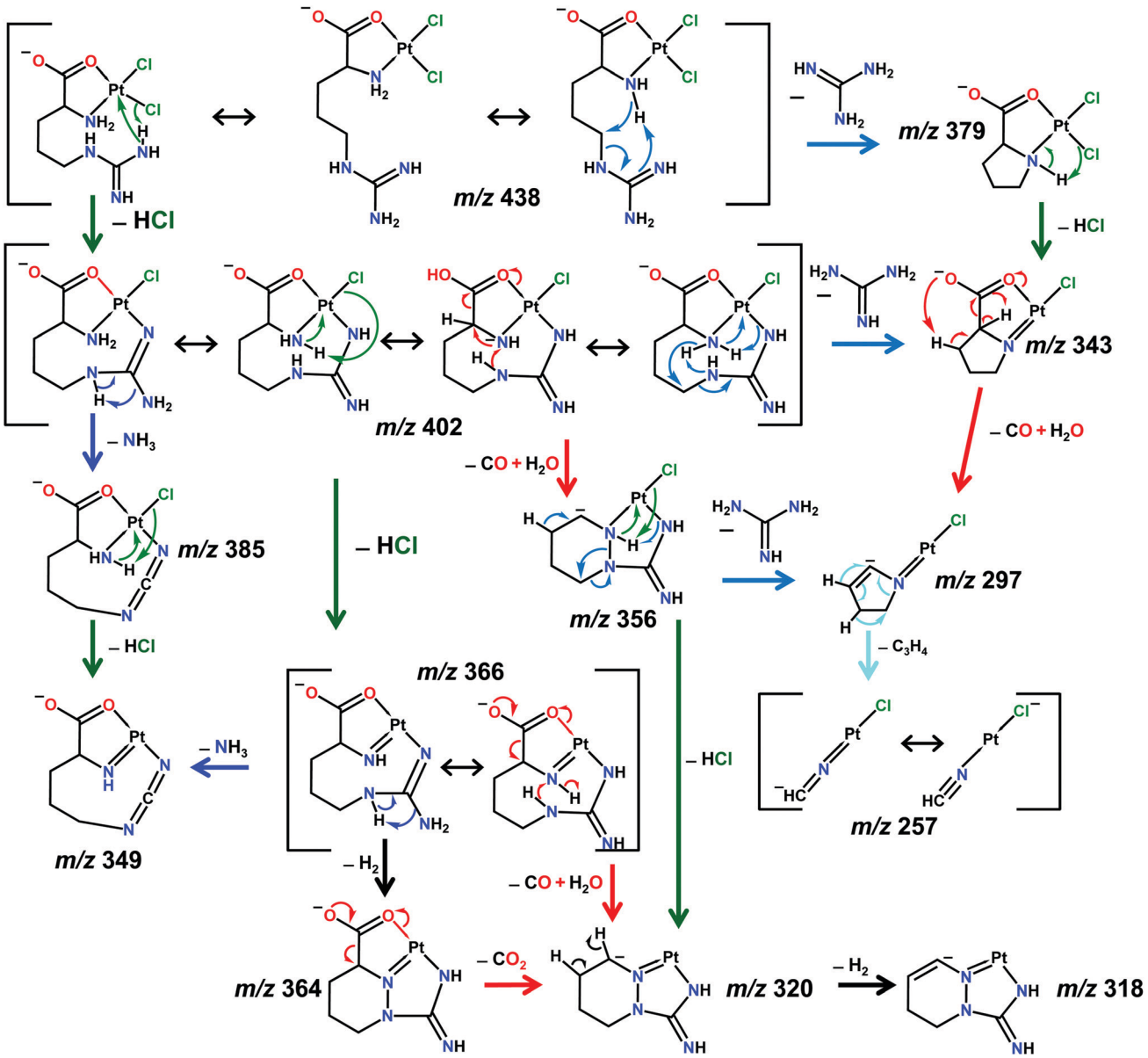

Scheme 1 Proposed fragmentation pathways of the $[(Arg-H)PtCl_2]^-$ complex.

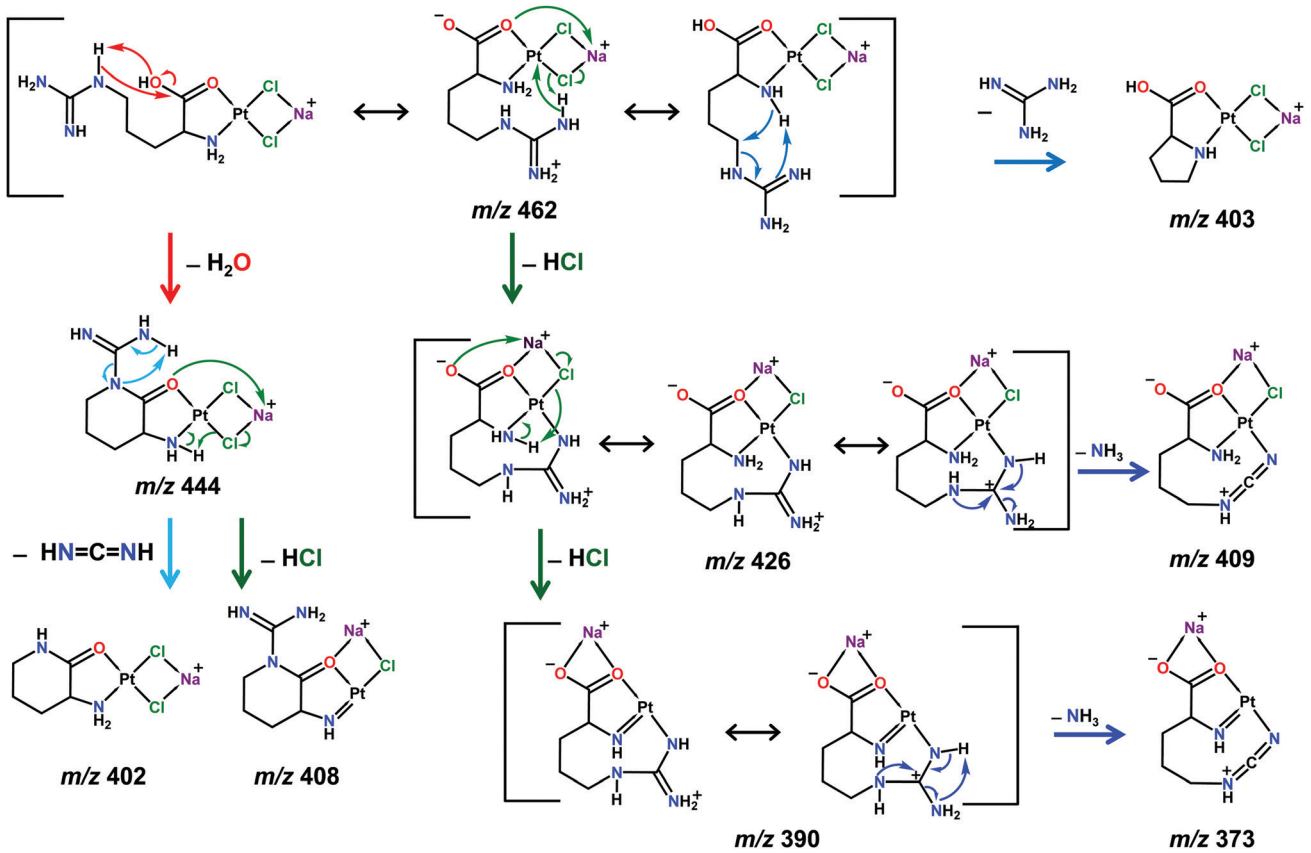

Scheme 2 Proposed fragmentation pathways of $[(Arg)PtCl_2 + Na]^+$ complex.

Arg in $[(Arg)PtCl_2 + Na]^+$, whereas $[(Arg–H)PtCl_2]^-$ lacks the excess proton shutting down this pathway. Water loss is one of the most common pathways that has been seen in the fragmentation of protonated arginine and several metal cationized arginine species,[57,59,62,65,66] and the sequential HN=C=NH loss was also observed previously for protonated arginine.[58] Interestingly, sequential loss of a second HCl was not observed for the $[(Arg)PtCl_2 + Na]^+$ complex after the water and HCl loss, and this is probably related to the lack of protons near the second chlorido ligand. The loss of guanidino group is another major dissociation pathway for the $[(Arg–H)PtCl_2]^-$ complex as well as one of the minor pathways for the $[(Arg)PtCl_2 + Na]^+$ complex. This neutral loss proposed to occur *via* 5-membered ring formation is commonly observed in the study of protonated and cationized arginine.[60–62] Ammonia loss was observed for both $[(Arg–H)PtCl_2]^-$ and $[(Arg)PtCl_2 + Na]^+$, but it is always a minor sequential pathway following elimination of one or two HCl. Ammonia loss was observed in many protonated and cationized arginine studies, and as the only fragmentation pathway for the Arg complexes with the Rb^+ and Cs^+ cations.[57,59,62,65,66] Isotopic labeling experiments suggest that NH_3 is eliminated from the guanidino side chain, and the proposed mechanism has been validated by theoretical calculations.[58,59,62] Thus, the NH_3 loss from Argplatin also likely arises from the guanidino group. A few additional minor fragments were observed for the $[(Arg–H)PtCl_2]^-$ complex, which is not surprising due to the high power provided by the FEL. Sequential loss of CO_2H_2 after elimination of one or two HCl or the guanidino group followed by one HCl from $[(Arg–H)PtCl_2]^-$ is observed, which is consistent with the CO loss accompanied by water loss commonly observed for arginine when interacting with a metal ion or 18-crown-6.[57,62,64] Other minor neutral elimination pathways such as H_2, CO_2, and C_3H_4 are all observed as sequential losses that occur after elimination of HCl or the guanidino group in the experiments for the $[(Arg–H)PtCl_2]^-$ complex with excessive laser power. The loss of CO_2 was also observed previously in the fragmentation of $[(Gly–H)PtCl_2]^-$.[25] These high energy intrinsic pathways are less likely to occur in solution. Overall, neutral loss of HCl or the guanidino group are major intrinsic fragmentation pathways of $[(Arg–H)PtCl_2]^-$, whereas HCl loss and water loss are the major intrinsic fragmentation pathways of the $[(Arg)PtCl_2 + Na]^+$ complex.

$[(Arg–H)PtCl_2]^-$ *vs.* $[(Gly–H)PtCl_2]^-$

The deprotonated Argplatin and Glyplatin complexes adopt similar binding modes of the amino acid to Pt, the backbone NO^- binding mode.[25] As can be seen in the comparison of IRMPD spectra of the $[(Arg–H)PtCl_2]^-$ and $[(Gly–H)PtCl_2]^-$ complexes in Fig. 2, the IR features in the fingerprint region are highly parallel, especially the peak position of the C=O stretch ($\sim$1670 cm^{-1}). However, this band is broad and quite asymmetric in the spectrum of the $[(Arg–H)PtCl_2]^-$ complex compared to that of $[(Gly–H)PtCl_2]^-$, which is probably a result

of the vibrations from the side chain guanidino group (Table 2). The C_ζ–N_ε stretch and N_ε–H bending provide the shoulder peaks near 1530 cm^{-1} for $[(Arg–H)PtCl_2]^-$ that are not observed for $[(Gly–H)PtCl_2]^-$, while the broader IR band in the range of 1255–1400 cm^{-1} of $[(Arg–H)PtCl_2]^-$ is due to the extra methylene groups along the side chain of Arg that are absent in Gly. The IR feature associated with backbone NH_2 wagging of $[(Gly–H)PtCl_2]^-$ at ~1030 cm^{-1} is blue shifted to ~1150 cm^{-1} in the IRMPD spectrum of $[(Arg–H)PtCl_2]^-$. A unique IR feature at ~800 cm^{-1} is observed only for $[(Arg–H)PtCl_2]^-$, which is associated with breathing of the (Arg–H)Pt chelation ring, due to the lack of these atoms in $[(Gly–H)PtCl_2]^-$. The clearly resolved backbone NH_2 stretches of $[(Gly–H)PtCl_2]^-$ become a single broad and intense feature in the spectrum of $[(Arg–H)PtCl_2]^-$. The carboxyl group is deprotonated in $[(Arg–H)PtCl_2]^-$, thus there is no O–H stretch (Fig. 3), and the side chain of Arg forms a variety of strong hydrogen-bonding interactions in the stable conformers populated that significantly broaden and flatten the IRMPD bands in the hydrogen-stretching region.[65,68,69] When these amino acid-linked platinum complexes chelate with nucleosides, Glyplatin may have the opportunity to coordinate to multiple sites due to its small size, whereas Argplatin may have the opportunity to form various hydrogen bonds with the nucleobase or sugar moieties of the nucleosides and thereby exhibit very different coordination preferences.

Argplatin in the gas *versus* the condensed phase

Spectroscopic and theoretical results suggest that Arg binds to Pt *via* the backbone amino and carboxylate moieties in both $[(Arg–H)PtCl_2]^-$ and $[(Arg)PtCl_2 + Na]^+$, consistent with the previously reported crystal structure of Argplatin.[21] However, in the gas phase the side chain of Arg is able to enhance stabilization *via* a number of hydrogen-bonding modes, whereas the Arg side chain is likely stabilized by interactions with solvent molecules in solution. In the case of $[(Arg–H)PtCl_2]^-$, the guanidino group may fold back to interact with Pt, the carboxylate moiety, or even a chlorido ligand, see Fig. 3. In the $[(Arg)PtCl_2 + Na]^+$ complex, hydrogen-bonding interactions between the side chain of Arg and the Pt center or the chlorido ligand are less likely to form as Arg is in its zwitterionic form. Instead hydrogen-bonding interactions between the protonated guanidino and deprotonated carboxylate moieties are found, see Fig. 4. The structure of $[(Arg)PtCl_2 + Na]^+$ in the gas phase probably represents the structure of Argplatin in solution better than that of $[(Arg–H)PtCl_2]^-$, because the net charge of Argplatin is likely to be zero in solution (pH = 7) with a positively charged side chain and a deprotonated carboxyl group.

The IR features observed for Argplatin in the gas phase are also consistent with the solid-phase IR results.[70] IR spectroscopy is an effective approach for distinguishing the NO^- binding conformers from the NN_s binding conformers of amino acid-linked platinum complexes. The carboxylic acid will produce a signature C=O band at ~1700 cm^{-1} in the fingerprint region and an O–H stretch in the hydrogen-stretching region, for example, the $\mathbf{NN_s\_A}$ conformer in $[(Arg)PtCl_2 + Na]^+$, see Fig. S11 (ESI†). However, if the carboxyl group is deprotonated, for example, in the solid-phase IR study or the $\mathbf{NN_s\_A}$ conformer of $[(Arg–H)PtCl_2]^-$, see Fig. S6 (ESI†), the obvious C=O and O–H stretches will be absent. Thus, charge manipulation in the gas phase is an important measure to distinguish the binding mode of amino acid-linked platinum complexes.

Conclusions

IRMPD action spectra for the $[(Arg–H)PtCl_2]^-$ and $[(Arg)PtCl_2 + Na]^+$ complexes were acquired in the IR fingerprint and hydrogen-stretching regions. HCl loss is the major fragmentation pathway, competing with guanidino group loss in $[(Arg–H)PtCl_2]^-$ or water loss in $[(Arg)PtCl_2 + Na]^+$. The predicted IR spectra of candidate structures calculated at the B3LYP/mDZP/def2-TZVP level of theory are compared with the experimental data. The preferred mode of binding of Arg to Pt is bidentate interaction with the backbone amino and carboxylate groups, NO^- binding, in both the $[(Arg–H)PtCl_2]^-$ and $[(Arg)PtCl_2 + Na]^+$ complexes. The guanidino group may fold back to gain additional stabilization *via* interaction with Pt, the carboxylate moiety, or even the chlorido ligand in $[(Arg–H)PtCl_2]^-$, whereas the guanidinium group of Argplatin generally forms hydrogen-bonding interactions with the carboxylate moiety in the $[(Arg)PtCl_2 + Na]^+$ complex. The most stable mode of sodium cation binding is bidentate interaction with the chlorido ligands roughly in the plane of the Pt center. The NO^- binding mode of Argplatin is consistent with that of Glyplatin, as well as the solid-phase results reported for Argplatin. IRMPD spectroscopic study in the gas phase with charge manipulation is an important measure to distinguish the binding mode of amino acid-linked platinum complexes and confirms that the Pt–Arg interaction is preserved under different pH and ionic strength environments.

Author contributions

M. T. R. (lead) administered this project and along with C. S. C. designed the project, research goals, aims, and acquired funding. M. T. R. (lead), C. S. C., J. M., G. B., and J. O. provided supervision and resources. B. K. synthesized the Argplatin complex. C. C. He (lead), L. A. H., H. A. R. Z. J. D, N. A. C., J. K. M., G. B., J. O., and M. T. R. performed the IRMPD action spectroscopy experiments. C. C. H. performed the electronic structure calculations and analyzed the data with assistance from M. T. R. C. C. H. wrote the original draft, and revised the manuscript with extensive feedback from M. T. R. (lead), G. B. and C. S. C.

Conflicts of interest

There are no conflicts to declare.

Acknowledgements

This work was financially supported by the National Science Foundation, under Grants OISE-0730072, OISE-1357787

(for the IRMPD measurements and international travel), DBI-0922819 (for the Bruker amaZon ETD QITMS employed in this work), CHE-1709789, the National Institutes of Health (GM087596), and a Paul A. Schaap Faculty Fellowship. C. C. H., L. A. H., and Z. J. D. thank Wayne State University for support *via* Thomas C. Rumble Graduate Research Fellowships. We thank Wayne State University C&IT for the computational resources and support. This work is part of the research program of FOM, which is financially supported by the Nederlandse Organisatie voor Wetenschappelijk Onderzoek (NWO). The skillful assistance of the FELIX staff is gratefully acknowledged.

References

1 B. Rosenberg, L. VanCamp, J. E. Trosko and V. H. Mansour, *Nature*, 1969, **222**, 385–386.
2 B. Rosenberg, L. VanCamp and T. Krigas, *Nature*, 1965, **205**, 698–699.
3 M. Kartalou and J. M. Essigmann, *Mutat. Res.-Fund. Mol. M.*, 2001, **478**, 1–21.
4 S. R. McWhinney, R. M. Goldberg and H. L. McLeod, *Mol. Cancer Ther.*, 2009, **8**, 10–16.
5 B. Lippert, *Cisplatin: Chemistry and Biochemistry of a Leading Anticancer Drug*, Wiley-VCH, Weinheim, Germany, 1999.
6 B. Rosenberg, *Interdiscipl. Sci. Rev.*, 1978, **3**, 134–147.
7 E. R. Jamieson and S. J. Lippard, *Chem. Rev.*, 1999, **99**, 2467–2498.
8 A. A. Hostetter, E. G. Chapman and V. J. DeRose, *J. Am. Chem. Soc.*, 2009, **131**, 9250–9257.
9 M. Hagerlof, P. Papsai, C. S. Chow and S. K. C. Elmroth, *J. Biol. Inorg. Chem.*, 2006, **11**, 974–990.
10 M. Galanski, M. A. Jakupec and B. K. Keppler, *Curr. Med. Chem.*, 2005, **12**, 2075–2094.
11 M. J. Cleare and J. D. Hoeschele, *Bioinorg. Chem.*, 1973, **2**, 187–210.
12 M. J. Cleare and J. D. Hoeschele, *Platin. Met. Rev.*, 1973, **17**, 2–13.
13 J. Holford, S. Y. Sharp, B. A. Murrer, M. Abrams and L. R. Kelland, *Brit. J. Cancer*, 1998, **77**, 366–373.
14 J. Reedijk, *Chem. Rev.*, 1999, **99**, 2499–2510.
15 L. R. Kelland, S. Y. Sharp, C. F. O'Neill, F. I. Raynaud, P. J. Beale and I. R. Judson, *J. Inorg. Biochem.*, 1999, **77**, 111–115.
16 X. Bao, PhD dissertation, Wayne State University, 2015, 1115, https://digitalcommons.wayne.edu/oa_dissertations/1115.
17 P. J. O'Dwyer, J. P. Stevenson and S. W. Johnson, *Drugs*, 2000, **59**, 19–27.
18 P. Beale, I. Judson, A. O'Donnell, J. Trigo, C. Rees, F. Raynaud, A. Turner, L. Simmons and L. Etterley, *Br. J. Cancer*, 2003, **88**, 1128–1134.
19 D. L. Nelson and M. M. Cox, *Lehninger Principles of Biochemistry*, 7th edn, W.H. Freeman and Company, New York, NY, 2017.
20 K. E. Sandman, P. Fuhrmann and S. J. Lippard, *J. Biol. Inorg. Chem.*, 1998, **3**, 74–80.
21 C. J. Ziegler, K. E. Sandman, C. H. Liang and S. J. Lippard, *J. Biol. Inorg. Chem.*, 1999, **4**, 402–411.
22 K. Rijal, X. Bao and C. S. Chow, *Chem. Commun.*, 2014, **50**, 3918–3920.
23 L. Dalla Via, O. Gia, S. M. Magno, A. Dolmella, D. Marton and V. Di Noto, *Inorg. Chim. Acta*, 2006, **359**, 4197–4206.
24 B. Kimutai, PhD dissertation, Wayne State University, 2020, 2360, https://digitalcommons.wayne.edu/oa_dissertations/2360.
25 C. C. He, B. Kimutai, X. Bao, L. Hamlow, Y. Zhu, S. F. Strobehn, J. Gao, G. Berden, J. Oomens and C. S. Chow, *et al.*, *J. Phys. Chem. A*, 2015, **119**, 10980–10987.
26 B. Kimutai, C. C. He, A. Roberts, M. L. Jones, X. Bao, J. Jiang, Z. Yang, M. T. Rodgers and C. S. Chow, *J. Biol. Inorg. Chem.*, 2019, **24**, 985–997.
27 D. Oepts, A. F. G. van der Meer and P. W. van Amersfoort, *Infrared Phys. Techn.*, 1995, **36**, 297–308.
28 J. Martens, G. Berden and J. Oomens, *Anal. Chem.*, 2016, **88**, 6126–6129.
29 J. Martens, J. Grzetic, G. Berden and J. Oomens, *Nat. Commun.*, 2016, **7**, 11754.
30 J. J. Valle, J. R. Eyler, J. Oomens, D. T. Moore, A. F. G. van der Meer, G. von Helden, G. Meijer, C. L. Hendrickson, A. G. Marshall and G. T. Blakney, *Rev. Sci. Instrum.*, 2005, **76**, 23103.
31 A. Bino, S. Cohen, J. Altman and M. Wilchek, *Inorg. Chim. Acta*, 1988, **147**, 99–102.
32 J. Altman, M. Wilchek and A. Warshawsky, *Inorg. Chim. Acta*, 1985, **107**, 165–168.
33 M. J. Frisch, G. W. Trucks, H. B. Schlegel, G. E. Scuseria, M. A. Robb, J. R. Cheeseman, G. Scalmani, V. Barone, B. Mennucci, G. A. Petersson, *et al.*, *Revision C.01 edn*, Gaussian, Inc., Wallingford, CT, USA, 2009.
34 D. Feller, *J. Comput. Chem.*, 1996, **17**, 1571–1586.
35 K. L. Schuchardt, B. T. Didier, T. Elsethagen, L. S. Sun, V. Gurumoorthi, J. Chase, J. Li and T. L. Windus, *J. Chem. Inf. Model.*, 2007, **47**, 1045–1052.
36 K. Wolinski, J. F. Hinton, D. S. Wishart, B. D. Sykes, F. M. Richards, A. Pastone, V. Saudek, P. D. Ellis, G. E. Maciel, J. W. McIver, Jr., *et al.*, *Hyperchem™ Professional Release 8.0.10*, Hypercube, Inc., Gainsville, FL, 2004.
37 D. Bertsimas and J. Tsitsiklis, *Stat. Sci.*, 1993, **8**, 10–15.
38 N. L. Allinger, *J. Am. Chem. Soc.*, 1977, **99**, 8127–8134.
39 T. R. Cundari, W. Fu, E. W. Moody, L. L. Slavin, L. A. Snyder, S. O. Sommerer and T. R. Klinckman, *J. Phys. Chem.*, 1996, **100**, 18057–18064.
40 T. R. Cundari and W. T. Fu, *THEOCHEM*, 1998, **425**, 51–60.
41 R. R. Wu, B. Yang, G. Berden, J. Oomens and M. T. Rodgers, *J. Phys. Chem. B*, 2014, **118**, 14774–14784.
42 R. R. Wu, B. Yang, G. Berden, J. Oomens and M. T. Rodgers, *J. Phys. Chem. B*, 2015, **119**, 2795–2805.
43 R. R. Wu, B. Yang, C. E. Frieler, G. Berden, J. Oomens and M. T. Rodgers, *J. Phys. Chem. B*, 2015, **119**, 5773–5784.
44 R. R. Wu, B. Yang, C. E. Frieler, G. Berden, J. Oomens and M. T. Rodgers, *Phys. Chem. Chem. Phys.*, 2015, **17**, 25978–25988.
45 R. R. Wu, B. Yang, C. E. Frieler, G. Berden, J. Oomens and M. T. Rodgers, *J. Am. Soc. Mass Spectrom.*, 2016, **27**, 410–421.

46 R. R. Wu, C. C. He, L. A. Hamlow, Y.-W. Nei, G. Berden, J. Oomens and M. T. Rodgers, *Phys. Chem. Chem. Phys.*, 2016, **18**, 15081–15090.
47 R. R. Wu, C. C. He, L. A. Hamlow, Y.-W. Nei, G. Berden, J. Oomens and M. T. Rodgers, *J. Phys. Chem. B*, 2016, **120**, 4616–4624.
48 C. C. He, L. A. Hamlow, Z. J. Devereaux, Y. Zhu, Y. W. Nei, L. Fan, C. P. McNary, P. Maitre, V. Steinmetz and B. Schindler, *et al.*, *J. Phys. Chem. B*, 2018, **122**, 9147–9160.
49 C. C. He, L. A. Hamlow, Y. Zhu, Y. W. Nei, L. Fan, C. P. McNary, P. Maitre, V. Steinmetz, B. Schindler and I. Compagnon, *et al.*, *J. Am. Soc. Mass Spectrom.*, 2019, **30**, 2318–2334.
50 P. B. Armentrout, Y. Chen and M. T. Rodgers, *J. Phys. Chem. A*, 2012, **116**, 3989–3999.
51 P. B. Armentrout, B. Yang and M. T. Rodgers, *J. Phys. Chem. B*, 2013, **117**, 3771–3781.
52 P. B. Armentrout, B. Yang and M. T. Rodgers, *J. Phys. Chem. B*, 2014, **118**, 4300–4314.
53 D. T. Moore, J. Oomens, L. van der Meer, G. von Helden, G. Meijer, J. Valle, A. G. Marshall and J. R. Eyler, *ChemPhysChem*, 2004, **5**, 740–743.
54 N. Heine, M. R. Fagiani, M. Rossi, T. Wende, G. Berden, V. Blum and K. R. Asmis, *J. Am. Chem. Soc.*, 2013, **135**, 8266–8273.
55 T. E. Cooper, J. T. O'Brien, E. R. Williams and P. B. Armentrout, *J. Phys. Chem. A*, 2010, **114**, 12646–12655.
56 C. S. Contreras, N. C. Polfer, J. Oomens, J. D. Steill, B. Bendiak and J. R. Eyler, *Int. J. Mass Spectrom.*, 2012, **330**, 285–294.
57 N. N. Dookeran, T. Yalcin and A. G. Harrison, *J. Mass Spectrom.*, 1996, **31**, 500–508.
58 M. J. Deery, S. G. Summerfield, A. Buzy and K. R. Jennings, *J. Am. Soc. Mass Spectrom.*, 1997, **8**, 253–261.
59 R. A. Jockusch, W. D. Price and E. R. Williams, *J. Phys. Chem. A*, 1999, **103**, 9266–9274.
60 F. Rogalewicz, Y. Hoppilliard and G. Ohanessian, *Int. J. Mass Spectrom.*, 2000, **195**, 565–590.
61 I. P. Csonka, B. Paizs and S. Suhai, *J. Mass Spectrom.*, 2004, **39**, 1025–1035.
62 P. Y. I. Shek, J. Zhao, Y. Ke, K. W. M. Siu and A. C. Hopkinson, *J. Phys. Chem. A*, 2006, **110**, 8282–8296.
63 T. Cai, J. Zhou, Y. Jiang, K. Xie, D. Fang, H. Qi and Z. Wu, *J. Mass Spectrom.*, 2018, **53**, 700–704.
64 Y. Chen and M. T. Rodgers, *J. Am. Chem. Soc.*, 2012, **134**, 5863–5875.
65 M. F. Bush, J. T. O'Brien, J. S. Prell, R. J. Saykally and E. R. Williams, *J. Am. Chem. Soc.*, 2007, **129**, 1612–1622.
66 M. W. Forbes, M. F. Bush, N. C. Polfer, J. Oomens, R. C. Dunbar, E. R. Williams and R. A. Jockusch, *J. Phys. Chem. A*, 2007, **111**, 11759–11770.
67 D. R. Bush, V. H. Wysocki and P. Y. Scaraffia, *J. Mass Spectrom.*, 2012, **47**, 1364–1371.
68 B. Yang, R. R. Wu, G. Berden, J. Oomens and M. T. Rodgers, *J. Phys. Chem. B*, 2013, **117**, 14191–14201.
69 N. C. Polfer and J. Oomens, *Mass Spectrom. Rev.*, 2009, **28**, 468–494.
70 C. C. He, PhD dissertation, Wayne State University, 2018, 2103, https://digitalcommons.wayne.edu/oa_dissertations/2103.